COMPARISONS OF MULTIPLE PHOTON COINCIDENCE IMAGING TECHNIQUES

Z. Liang and R. Jaszczak

Department of Radiology, Nuclear Medicine Division
Duke University Medical Center, Durham, NC 27710

ABSTRACT

We compare analytically techniques for multiple-photon coincidence imaging in terms of spatial resolution, detector efficiency (or simply efficiency), and system sensitivity for a spherical water phantom (or simply sensitivity). One analysis consists of comparing photon-photon coincidence single-photon-emission computerized tomography (PP-SPECT) with angularly unconstrained, electronically collimated triple-photon coincidence imaging technique (TPCIT). A second analysis compares positron-emission tomography using time-of-flight information (TOF-PET) with angularly constrained, electronically collimated TPCIT. The angularly unconstrained TPCIT has similar spatial resolution, higher efficiency, and higher sensitivity, as compared with PP-SPECT. The angularly constrained TPCIT has similar spatial resolution, lower efficiency, and lower sensitivity, as compared with TOF-PET. However, the angularly constrained TPCIT can, for brain imaging, reduce the localization range of photon-emission sites along projection rays from about 20 *cm* to about 1 *cm* during data acquisition while TOF-PET currently reduces the range to about 7 *cm*.

INTRODUCTION

Single-photon emission computerized tomography (SPECT) and positron emission tomography (PET) have been extensively investigated [1-4]. For both of these modalities, images are reconstructed from projection ray-sums (or simply projections). A projection ray-sum is the summation of photon-emission intensities along the corresponding projection ray (i.e. the number of photons detected in a finite time interval along the projection ray). The photons detected for the projection ray are assumed to be emitted anywhere along the projection ray. It has been shown that signal-to-noise ratio (SNR) of reconstructed images can be improved if photon-emission sites are localized, during data acquisition, in a shorter range along projection rays, such as PET using time-of-flight (TOF) information (TOF-PET) [5] and photon-photon coincidence SPECT (PP-SPECT) [6].

1. *PP-SPECT*

As shown in Fig.1, the detector system of PP-SPECT is arranged to detect, in coincidence, two angularly unconstrained photons (i.e., the angle subtended by the two simultaneously emitted photons can vary from event to event) with mechanic collimation of lead collimators. Ideally, two projection lines are provided by the collimator holes for a coincidence event. If the two lines are not in the same direction, the intersection of the two lines determines the emission site of the two coincidence photons. The radioisotope distribution that emitted the two (or more) angularly unconstrained photons simultaneously is then assembled by the intersections of the lines. For collimator holes having finite sizes, the intersection of two projection rays determines a small volume. Image is then reconstructed from the small volumes.

Examples of radioisotopes that emit two or more angularly unconstrained photons simultaneously suitable to PP-SPECT are given below:

$$K_{19}^{43} \quad Cr_{24}^{48} \quad Se_{34}^{73} \quad Se_{34}^{75} \quad Br_{37}^{82} \quad Rh_{45}^{101}$$
$$Cd_{48}^{109} \quad I_{53}^{130} \quad Ce_{58}^{139} \quad Sm_{62}^{145} \quad Ta_{73}^{178} \quad Ir_{77}^{192}.$$

PP-SPECT improves significantly the localization range of photon emissions ($\approx$ 1 *cm*). The difficulty with it is the low detection efficiency due to the use of lead collimators ($\approx 10^{-8}$) [7-8]. In order to increase the efficiency while maintaining a comparable localization range, an angularly unconstrained triple-photon coincidence imaging technique (u-TPCIT) was studied [9-10].

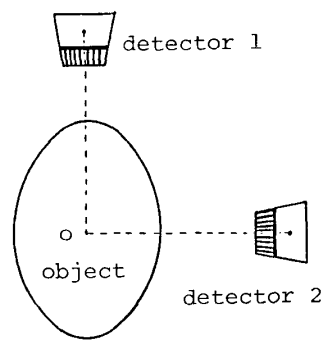

Fig.1: Two photons emitted simultaneously at site *O* are detected, in coincidence, by two γ-cameras. The intersecting volume of the two projection rays determines the localization range of photon-emission site around point *O*.

0018-9499/90/0600-1282$01.00

2. *u-TPCIT*

In the angularly unconstrained TPCIT of Fig.2, a radioisotope emits three or more angularly unconstrained photons simultaneously. Each photon is detected using electronic collimation (Fig.3) and generates ideally a cone surface in the patient space [11-12]. Three photons are detected in coincidence and generate three cone surfaces. The intersection of the three cone surfaces determines the location of the emission site. The image is then assembled using the intersecting points. In practice, electronic collimation generates hollow cones due to finite energy and spatial resolutions of detectors (Fig.4) [12]. The image is then reconstructed using the intersecting volumes of the hollow cones. If only one photon is considered, u-TPCIT is identical to the electronically collimated SPECT (EC-SPECT) [12] and the image is reconstructed from the hollow cones.

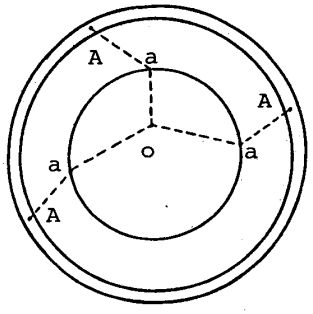

Fig.2: Three photons emitted simultaneously at site O are detected each, in coincidence, using electronic collimation (see Fig.3). The intersection of the three cone surfaces determines the localization range of photon-emission site around point O.

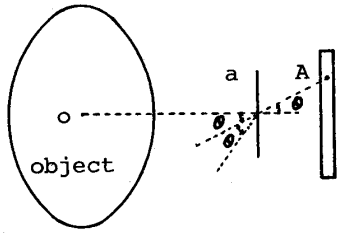

Fig.3: A photon emitted at site O is scattered within the thin detector (a) and is absorbed by the thick detector (A). θ is the scatter angle. The two interaction sites within the thin and thick detectors and the scatter angle determine a cone surface in the object space. 2θ is the conic angle.

As shown in Fig.4, a photon emerging from patient's body is scattered in a thin detector [depositing energy $E(a)$ at position $X(a)$] and absorbed in a thick detector [depositing energy $E(A)$ at position $X(A)$]. The thin and thick detectors of a detector stack of Fig.4 are able to detect in coincidence the photon that deposits the energy

$$E_0 = E(a) + E(A) \qquad (1)$$

to the stack. This energy sum is used to attempt to determine whether the photon has been scattered or not within the body. The conic angle θ is determined by the energy $E(a)$ [and/or combining with $E(A)$] using the Compton scatter formula [11-12]. The thickness of the hollow cone $\Delta\theta$ is a function of the separation h, the energy and spatial resolutions of the thin and thick detectors. Due to angular correlations of the three simultaneous photons (i.e., the three photons are not in a same direction), the intersecting volume is determined by the intersection of the three hollow cones in different angles. The localization range is about 1 *cm* [9,12], which is comparable to that of PP-SPECT.

A double hexagonal or ring detector system (Fig.2) or a truncated spherical detector system (Fig.5) [9-10,13-14] can be assembled using many small thin-thick detector stacks (Fig.3). The thin detector should have high energy resolution and be relatively fast, e.g., *HpGe* (with energy resolution ΔE = 2.27 *Kev* for 140 *Kev* and time resolution δt = 0.4 *nsec* for 511 *Kev* photons) [15-20], or a plastic scintillator [21-22]. If *HpGe* is used, the size of the thin-detector element may be chosen as $3\times3\times6$ mm^3 [9,13]. The thick detector should have high stopping power and possess good energy resolution, e.g., *BGO* (for 511 *Kev* photons, efficiency η_0 = 77% and $\Delta E \leq 15\%$) [15-16]. The inner ring of Fig.2 has a radius of d, the outer one has a radius of $d + h$, and both the rings have a length of $2z_0$. A truncated spherical detector system would be optimal for brain imaging [10,14]. The readout for the inner thin detector may employ the technique described in [23]. The position sensitive technique described in [24] may be used for the readout of the outer thick detector. The outer thick detector of the ring may be a conventional PET system. The efficiency of u-TPCIT for detecting three photons of 140 *Kev* with the truncated spherical detector of Fig.5 is about 10^{-4} [9,12], which is significantly improved as compared with PP-SPECT.

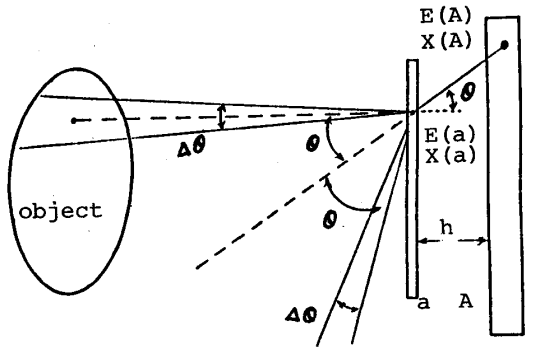

Fig.4: Electronic collimation process of scattering in a thin detector (a) and absorption in a thick detector (A). $E(a)$ and $E(A)$ are the energies detected by the thin and thick detectors, respectively. $X(a)$ and $X(A)$ are the positions measured by the thin and thick detectors, respectively. θ is the scatter angle and h the separation of the thin and thick detectors. A hollow cone is determined by its axis passing through the points $X(a)$ and $X(A)$, its apex at the point $X(a)$, its conic angle 2θ, and the angular uncertainty $\Delta\theta$. The likelihood of the scattering-absorption event for a photon is given by Eq.(11).

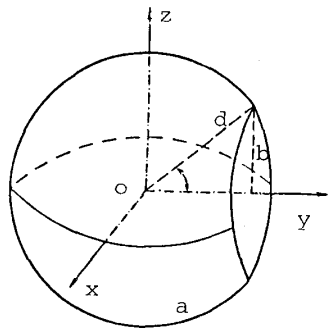

Fig.5: A truncated spherical detector system consisting of two layers of a thin and a thick detectors. The inner thin-detector layer (a) has a radius of d. The outer thick-detector layer (A) has a radius of $d + h$. The outer thick-detector layer (A) is not shown. The truncating circle has a radius of b.

However, random coincidences with u-TPCIT can cause image degradation. The random coincidences consist of two parts: (1) the random coincidences of the thin and thick detectors for a photon detection in a single detector stack [11-12]:

$$R_c \approx 2\tau_1 R_1 R_2 \qquad (2)$$

where R_c is the random-coincidence rate of the thin-thick detector stack, R_1 and R_2 are the single rates of the thin and thick detectors respectively and τ_1 is the coincidence resolving time; and (2) the random coincidences among the thin detectors for triple-photon detection in three detector stacks:

$$R_{cc} \approx 3\tau_2 R_1^3 \qquad (3)$$

where R_{cc} is the random-coincidence rate of three detector stacks. The resolving time τ_2 may be different from τ_1. Noise characteristics of a single detector stack for electronic collimation has been investigated in [25]. The noise propagation of TPCIT can be studied in a similar manner.

Since there is no lead collimator in front of the thin detector, scattered photons within the patient's body produce a rather high noise background. Some of these scattered photons can be rejected by the sum of energies from the thin and thick detector in a stack, provided that the detectors possess good energy resolution and are relative fast. There are two kinds of multiple-scatter processes: a photon may experience multiple scatters within the thin detector and then is absorbed in the thick detector; or a photon may experience multiple scatters within the thick detector and is then back-scattered to the thin detector and is absorbed there. Part of these multiple-scatter events can be removed using the detected energies $E(a)$ and $E(A)$. For example, the energy $E(a)$ in the forward scattering has a maximal value $E_m(a)$ at $\theta = 90$ degree. When the detected $E(a)$ is greater than $E_m(a)$, the event is rejected. Some photons may have been scattered more than once within the thin detector and deposit energy $E(a)$ greater than $E_m(a)$. These photons will be rejected. The single back-scattered photons from thick detector back to thin detector have energy greater than $E_m(a)$. If these back-scattered photons are absorbed in thin detector, they will be rejected. All of the random effects above result in image degradation. Monte Carlo modeling can be used to investigate these random effects.

Both of u-TPCIT and PP-SPECT modalities use angularly unconstrained photons. The radioisotopes suitable to u-TPCIT are also suitable to PP-SPECT. Examples of radioisotopes that emit three or more angularly unconstrained photons simultaneously are:

Ni_{28}^{56}	Zn_{30}^{71m}	Tc_{43}^{94}	Ag_{47}^{100}	In_{49}^{104}	Cs_{55}^{120}
Cs_{55}^{122}	Sb_{51}^{126}	Sb_{51}^{126m}	Sb_{51}^{128m}	I_{53}^{130}	Gd_{64}^{146}
Ho_{67}^{156}	Ho_{67}^{164m}	Lu_{71}^{174m}	Lu_{71}^{178m}	Ta_{73}^{178}	Hf_{72}^{180m}
Hf_{72}^{182m}	Ta_{73}^{182m}	Ti_{81}^{194m}	Au_{79}^{196m2}	At_{85}^{202}	At_{85}^{204} .

A few of these radioisotopes are described in table 1 in terms of half-life, abundance, energy, production, labeling characteristics, biologic effects, and dose consideration. As an example, the decay schems of isotope Hf_{72}^{182m} is shown by Fig.6 [26]. It emits three photons simultaneously of energies 224, 344, and 455 (or 507) *Kev*, respectively.

Table 1

The nuclides that emit three or more single-photons simultaneously are:

nuclide	half-life	γ_1	γ_2	γ_3	γ_4
$Sb_{51}^{126(m)}$	19.00m	695.00(85%)	666.33(85%)	414.80(85%)	
I_{53}^{130}	12.36h	739.48(90%)	668.54(90%)	536.09(90%)	
Gd_{64}^{146}	48.30d	154.58(77%)	115.52(77%)	114.67(70%)	
$Lu_{71}^{178(m)}$	23.00m	426.36(100%)	325.56(100%)	213.43(100%)	93.18(100%)
Ta_{73}^{178}	2.40h	426.36(100%)	325.56(100%)	213.43(100%)	93.18(100%)
$Hf_{72}^{180(m)}$	5.50h	443.20(79%)	332.30(100%)	215.24(100%)	93.18(100%)
		500.70(21%)			
$Hf_{72}^{182(m)}$	62.00m	506.60(64%)	344.10(100%)	224.40(100%)	97.60(100%)
		455.80(36%)			
$Au_{79}^{196(m2)}$	9.70h	188.23(50%)	174.87(100%)	147.70(100%)	
		168.33(36.5%)	137.65(11.5%)		

nuclide	production	labeling characteristics	biologic effects	dose considerations
$Sb_{51}^{126(m)}$	$Te^{126}(n,p)$	not known	not known	o.k.
I_{53}^{130}	$I^{129}(n,\gamma)$	very good	very good	o.k.
Gd_{64}^{146}	$Sm^{144}(\alpha,2n)$	not known	not known	o.k.
$Lu_{71}^{178(m)}$	$Ta^{181}(n,\alpha)$ parent Hf^{178m1}	not known	not known	good
Ta_{73}^{178}	$Lu^{175}(\alpha,n)$ parent Hf^{178m1}	not known	not known	good
$Hf_{72}^{180(m)}$	$Hf^{179}(n,\gamma)$	not known	not known	very good
$Hf_{72}^{182(m)}$	$W^{186}(p,p\alpha)$ parent Ta^{182}	not known	not known	very good
$Au_{79}^{196(m2)}$	$Pt^{196}(d,2n)$	not known	not known	very good

3. *TOF-PET*

As shown in Fig.7, since the two angularly constrained pair-photons are emitted in 180-degree opposite directions ideally, the difference in arrival times between the two 511 *Kev* photons can be used to shorten the localization range of emission site around x. TOF can reduce, for brain imaging, the range of annihilation events on the projection rays

effectively from 20 *cm* to about 7 *cm* [27-28]. In order to achieve the sub-nanosecond resolving times, however, high-speed low-sensitivity detector materials are used [15,27] and energy resolution may tend to be compromised. For example, BaF_2 (with time resolution δt = 0.3 *nsec* and efficiency η_0 = 60%) is used for TOF-PET rather than *BGO* (δt = 5, η_0 = 77%) which is used in conventional PET. Other materials that might be considered for TOF-PET are [15]:

CsF (δt = 0.4 , η_0 = 50%)
Liquid Xenon (δt = 0.2 , η_0 = 49%)
HpGe (δt = 0.4 , η_0 = 53%)
CdTe (δt = 0.8 , η_0 = 66%).

All of these materials have lower efficiency, as compared to *BGO*. To avoid the limitation of lower efficiency, a composite detector system was proposed [16] in which the high-speed low-sensitivity detectors (required for TOF resolving time) are backed by high-sensitivity lower speed detectors (for adequate energy resolution). By using extremely fast detectors and appropriate coincidence electronics, the localization range can be improved to about 5 *cm* [15,21,29]. Further improvement is seriously limited by the detector materials and coincidence electronics. An angularly constrained TPCIT (c-TPCIT) which has the potential to reduce the localization range to about 1 *cm* has been proposed [9,30]. Preliminary studies on this technique were reported in [10].

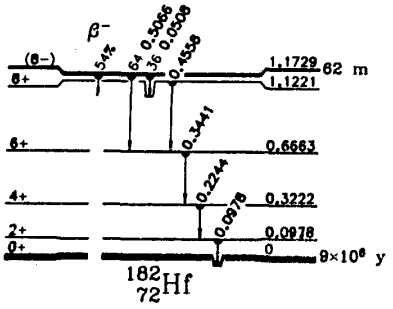

Fig.6: The decay scheme of isotope Hf_{72}^{182m}.

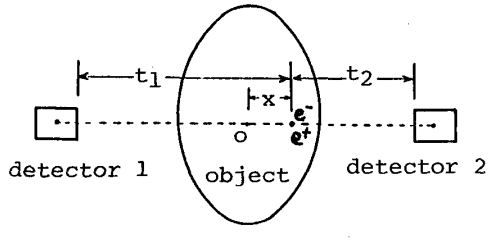

$$x = (t_1 - t_2) \, c \, / \, 2$$

Fig.7: The difference in arrival times (t_1 - t_2) between pair-photons at two detectors respectively can determine the site of a positron-annihilation event, where c is the speed of light and x the distance of the annihilation site from the center of detector system.

4. *c-TPCIT*

In the angularly constrained TPCIT of Fig.8, a radioisotope emits a positron and one or more single-photons simultaneously. The positron annihilates with an electron and produces two back-to-back angularly constrained pair-photons. The pair-photons generate similar projections as that of conventional PET, or TOF-PET if TOF information is considered. Ideally, the projection rays are lines as shown in Fig.7 for two detector elements. The projection lines for coincidence events of c-TPCIT within three or four detector elements in two detector stacks (Fig.3) are shown in Fig.9. The single-photon is detected using electronic collimation. Ideally, the single-photon event generates a cone surface as described in Fig.3. The projection line from the pair-photons and the cone surface from the single-photon event intersect at two points. Since the most likely Compton scatter angle is about θ = 50 *degree* for typical detector materials [15,29], the separation of the two intersecting points can be in the order of a few *cm*. For brain imaging, one intersection will usually be out of the brain region. If TOF is also used, a single intersection is always ensured. Considering the uncertainties due to measurements, the localization range of an emission site is the intersection of a cylinder (generated by the pair-photons) and a hollow cone (generated by the single-photon). The length of the cylinder segment intersected by the hollow cone is about 1 *cm* [9,12] for intersections at right angles. Comparing with TOF-PET, the localization range is significantly improved.

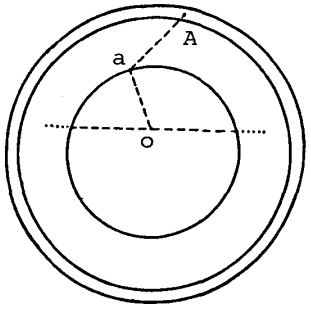

Fig.8: A positron and a single-photon are emitted simultaneously at site *O*. The single-photon is detected by a detector stack (*a*-*A*) of Fig.3 using electronic collimation. The positron annihilates with an electron and produces two back-to-back angularly constrained pair-photons. The detection of the pair-photons is depicted by Fig.9. The single-photon and pair-photons are detected in coincidence. The intersections of the cone surface from the single-photon and the line from the pair-photons determine the localization range of photon-emission sites.

The pair-photon coincidence event within the detector system of Fig.8 is detected in two detector stacks. There are six classes of pair-photon coincidence event, which generate the cylinders as conventional PET or TOF-PET does. These classes of coincidence event are depicted in Fig.9. Class (c) corresponds to conventional PET or TOF-PET.

The other five classes of (a)-(b) and (d)-(f) associated with the thin detector will improve detection efficiency. The ratio of the likelihood of the 5 classes to the PET class (c) is about 16% [10,13]. Considering the decrease in efficiency due to the single-photon detection and the increase due to the thin detector, the efficiency of c-TPCIT using the truncated spherical detector of Fig.5 is lowered to about 25% of TOF-PET which uses the outer-ring detector of Fig.8 with multiple slices (for details about multiple-slice ring detector of PET, see reference [31]). We will discuss the trade-off between localization range and efficiency later.

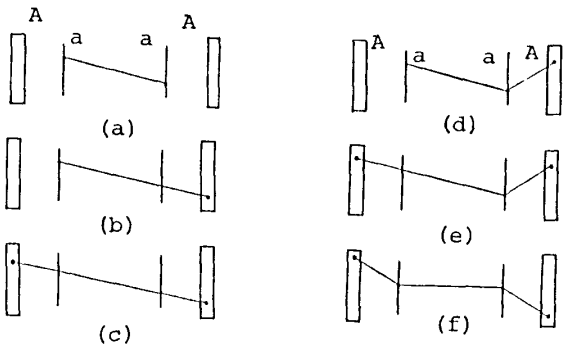

Fig.9: Diagrams of different cases of coincidence measurements of pair-photons from positron annihilations. (a), (b) and (c) represent 2-fold coincidence events (thick and thick, thick and thin, thin and thin). (c) corresponds to conventional PET detection. (d) and (e) are 3-fold coincidence events (thick-thin and thin, or thick). (f) stands for a 4-fold coincidence event (thick-thin and thin-thick). The likelihoods of each of these multiple-detector coincidence events are given by Eq.(12).

Since both of c-TPCIT and TOF-PET use the angularly constrained pair-photons, the radioisotopes suitable to c-TPCIT could also be used for TOF-PET. Examples of radioisotopes that emit a positron and one or more angularly unconstrained single-photons simultaneously are:

Sc_{21}^{42m}	Mn_{25}^{50m}	Fe_{26}^{52}	Fe_{26}^{53}	Co_{27}^{54m}	Co_{27}^{55}
Cu_{29}^{60}	Zn_{30}^{60}	Zn_{30}^{62}	Ga_{31}^{65}	Ga_{32}^{67}	As_{33}^{70}
As_{33}^{72}	Se_{34}^{73}	Br_{35}^{75}	Kr_{36}^{77}	Tc_{43}^{94m}	Rh_{45}^{98m}
Rh_{45}^{98m}	Ag_{47}^{100}	Ag_{47}^{101}	In_{49}^{104}	I_{53}^{120}	Cs_{55}^{120}
Cs_{55}^{122}	Cs_{55}^{126}	Pr_{59}^{132}	Pr_{59}^{134}	Pr_{59}^{136}	Pm_{61}^{136}
Ho_{67}^{152}	Ho_{67}^{154}	Ho_{67}^{156}	Ho_{67}^{157}	Ta_{73}^{168}	Ta_{73}^{170}
Re_{75}^{174}	Ti_{81}^{190}	Bi_{83}^{194} .			

The characteristics of a few of the radioisotopes for c-TPCIT are given in detail in table 2. The radioisotopes of I_{53}^{120}, Fe_{26}^{52}, and Br_{35}^{75} have been used already for clinical study. Because of what is already known about their chemistry at low concentration, these three radioisotopes may be the ones which offer the most potential for use with this imaging approach. Fig.10 shows the decay scheme of isotope Fe_{26}^{56} [26]. It emits a positron and a single-photon of energy 168 *Kev* simultaneously. The single-photon of energy 377 *Kev* is emitted with a delay of 21 minutes and does not affect the triple-photon event.

Table 2

The nuclides that emit a positron and one or more single-photons simultaneously are:

nuclide	half-life	positron	γ_1	γ_2	γ_3
$Sc_{21}^{42(m)}$	62.00s	100%	437.50(100%)	1227.0(100%)	1524.6(100%)
$Mn_{25}^{50(m)}$	1.74m	100%	783.30(100%)	661.50(28%)	
Fe_{26}^{52}	8.27h	57%	168.68(100%)		
$Co_{27}^{54(m)}$	1.46m	100%	411.00(100%)	1130.0(100%)	1407.0(100%)
Ge_{32}^{67}	19.00m	83%	167.00(100%)		
Se_{34}^{73}	7.10h	95%	360.90(100%)		
Br_{35}^{75}	98.00m	84%	286.50(77%)	141.20(4%)	431.00(4%)
Kr_{36}^{77}	75.00m	94%	129.70(92%)	276.00(3%)	312.00(3%)
Ho_{67}^{154}	12.00m	96%	334.50(89%)	570.00(21%)	158.00(7%)

nuclide	production	labeling characteristics	biologic effects	dose considerations
$Sc_{21}^{42(m)}$	$K^{39}(\alpha,n)$	not known	not known	good
$Mn_{25}^{50(m)}$	$Cr^{50}(p,n)$	not known	not known	good
Fe_{26}^{52}	$Cr^{50}(\alpha,2n)$ parent Mn^{52m}	very good	very good	o.k.
$Co_{27}^{54(m)}$	$Fe^{54}(p,n)$	not known	not known	good
Ge_{32}^{67}	$Zn^{64}(\alpha,n)$	not known	not known	o.k.
Se_{34}^{73}	$Ge^{70}(\alpha,n)$	not known	not known	good
Br_{35}^{75}	$Se^{70}(d,n)$	very good	very good	o.k.
Kr_{36}^{77}	$Br^{79}(p,3n)$ parent Br^{77}	not known	not known	good
Ho_{67}^{154}	$Dy^{156}(p,3n)$	not known	not known	good

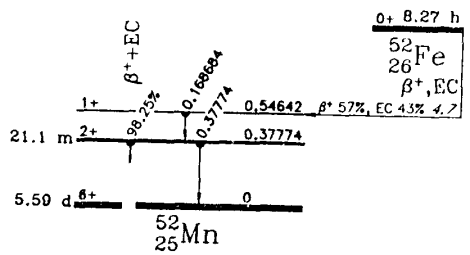

Fig.10: The decay scheme of isotope Fe_{26}^{52}.

We have previously studied the two imaging modes of u-TPCIT and c-TPCIT and compared them with conventional SPECT and PET, respectively [10]. In this paper, we evaluate these two imaging modes quantitatively in terms of spatial resolution, detector efficiency, and system sensitivity for a cylindrical water phantom. Comparisons of u-TPCIT with PP-SPECT and c-TPCIT with TOF-PET are carried out using these three factors. The results are presented in the following sections.

In order to facilitate the comparison studies, a few notations are defined below:

I:	localization range of photon-emission sites
P:	likelihood of photon detection or detector efficiency
S:	system sensitivity for water phantom or sensitivity.

Correspondingly, $I_{tof\text{-}pet}$, $P_{tof\text{-}pet}$, and $S_{tof\text{-}pet}$ are defined for TOF-PET. Similar definitions are used for u-TPCIT and c-TPCIT, respectively. The ratio S/I will be used later to

study the trade-off between S and I and to estimate the gain achieved in image quality characterized by SNR [32].

SPATIAL RESOLUTION

The spatial resolution of conventional SPECT is determined by the convolution of collimator resolution and the intrinsic spatial resolution of *NaI (Tl)* scintillation crystal. If the intrinsic spatial resolution is *FWHM* = 3.3 *mm*, the spatial resolution for super high-, ultra high-, and high-resolution collimators at different depths are given below [33]:

Table 3

Depth(*cm*)	SHR(*mm*)	UHR(*mm*)	HR(*mm*)
0	3.74	3.79	3.85
10	6.14	6.98	8.25
15	7.64	8.93	10.88
hole diameter	1.397	1.397	1.397
thickness	44.45	34.93	26.99

The spatial resolution for electronic collimation shown in Fig.4 is essentially determined by the bluring effects due to the size and energy resolution of the thin-detector element, and the intrinsic spatial resolution of the thick detector in the stack of Fig.3 [11-12]. The mathematical formulas to determine the bluring effects were given in [12] and are expressed as follows using notations suitable to this paper.

Let $t \times t$ denote the area of the thin-detector elements, the angular bluring $\Delta\theta_1$ due to the finite size t is given by solving the equation

$$h \cdot \tan(\theta + \Delta\theta_1) = h \cdot \tan(\theta + \omega) + t/2 \qquad (4)$$

at a scatter angle θ, where 2ω is the angle subtended by t; $\tan(\omega) = (0.5\,t/d)$, d is the distance from the thin-detector element to a point in patient space at which the resolution is to be determined, and h is the separation of the thin and thick detectors.

Let l denote the thickness of the thin-detector element, the angular bluring $\Delta\theta_2$ due to the finite thickness l is given by solving the equation

$$h \cdot \tan(\theta + \Delta\theta_2) = (h + l/2)\tan(\theta) \qquad (5)$$

at the scatter angle θ.

The angular bluring $\Delta\theta_3$ due to the intrinsic spatial resolution $FWHM = w$ of the thick detector is determined by the equation

$$h \cdot \tan(\theta + \Delta\theta_3) = h \cdot \tan(\theta) + w/2 \qquad (6)$$

at the scatter angle θ. If $t = 3$, $l = 6$ and $w = 3$ *mm*, and $h = 5$ and $d = 15$ *cm* are chosen, $\Delta\theta_1 = 1.256154$, $\Delta\theta_2 = 1.634741$, and $\Delta\theta_3 = 0.699821$ for scatter angle $\theta = 50$ *degrees*.

The relation between the scattered energy E and the scatter angle θ for Compton interaction determines the angular bluring $\Delta\theta_4$ due to the finite energy resolution ΔE of the thin-detector element. The relation is expressed as:

$$E = \hbar\nu \frac{a(1 - \cos(\theta))}{1 + a(1 - \cos(\theta))} \qquad (7)$$

where $a = \hbar\nu(Kev)/511$ and $\hbar\nu$ is the energy of primary photon. The angular bluring $\Delta\theta_4$ is given by $\Delta\theta_4 = (\partial\theta / \partial E)\Delta E$. If the energy resolution of the thin-detector element is 2.27 *Kev* [12], $\Delta\theta_4 = 4.707007$ and 1.410712 *degrees* for $E = 150$ and 300 *Kev*, respectively, at scatter angle $\theta = 50$ *degrees*.

It is clear that the total angular bluring is dominated by $\Delta\theta_4$ for lower energies (< 300 *Kev*) and by $\Delta\theta_2$ for higher energies (> 300 *Kev*). The four bluring factors result in a total angular resolution $\Delta\theta$ for electronic collimation of Fig.4 of

$$\tan^2(\Delta\theta) = \sum_{i=1}^{4} \tan^2(\Delta\theta_i). \qquad (8)$$

For u-TPCIT with the least photon energy $E = 224$ *Kev* (which results in worst bluring) among the three coincidence photons of Fig.6, $\Delta\theta_4 = 2.209836$ and $\Delta\theta = 3.100240$ for scatter angle $\theta = 50$ *degrees*. The linear resolution at a distance of 15 *cm* from the thin-detector element is then about *FWHM* = 8 *mm*. In c-TPCIT mode, if the single-photon has $E = 168$ *Kev* as shown in Fig.10, $\Delta\theta_4 = 3.757958$, and $\Delta\theta = 4.339662$ *degrees*. The linear resolution at the distance of 15 *cm* is about *FWHM* = 11 *mm*. If the energy resolution ΔE could be reduced to 1.5 *Kev* by using a detector material other than *HpGe* and *BGO* or using the relation of (1) to refine the energy-detection uncertainty [where the incident photon energy is accurately known from decay process and $E(a)$ and $E(A)$ are measured seperately], then the angular resolutions are $\Delta\theta = 2.62025$ *degrees* for 224 *Kev* and 3.30032 for 168 *Kev*. The linear resolutions are, therefore, 6.8 *mm* and 8.6 *mm* respectively.

Referring to table 3, the spatial resolution of u-TPCIT is comparable to that of conventional SPECT. The size of the intersecting small volume of three hollow-cones for u-TPCIT is comparable to that of two-cylinder intersection for PP-SPECT, i.e., $I_{u\text{-}tpcit} \approx I_{pp\text{-}spect} \approx 1$ *cm*. If the u-TPCIT has higher sensitivity, it is expected that u-TPCIT would produce better images.

If the outer ring detector of c-TPCIT (Fig.8) is a TOF-PET device, the spatial resolution of c-TPCIT is comparable to that of TOF-PET. Currently TOF information can reduce the localization range of an isotope-decay event to about $I_{tof\text{-}pet} = 7$ *cm*. For c-TPCIT with a positron and a 168 *Kev* single-photon decay process, the intersection length of the cylinder and hollow cone at normal angle is about 1 *cm*. In another words, the localization range of an isotope-decay event of c-TPCIT is about $I_{c\text{-}tpcit} = 1$ *cm*. The localization range is significantly improved. However, since c-TPCIT has lower sensitivity, the reconstructed image may be compromised. Monte Carlo simultaneous may provide a quantitative indication of the advantages and disadvantages of c-TPCIT.

DETECTOR EFFICIENCY

The detector efficiency is calculated for a point source in air at the center of detector system. For u-TPCIT and c-TPCIT, the truncated spherical detector system of Fig.5 is considered. The radius of the inner thin detector is d = 15 cm. It may be constructed of $HpGe$ semiconducting material. The outer thick detector has a radius of $d + h$ = 20 cm and may be made of BGO scintillation material. In Fig.5, the outer thick detector is not shown. The truncated part is a ring with a radius of b = 10 cm. The detector system of PP-SPECT consists of five γ-cameras which resemble approximately the truncated sphere of Fig.5. The detector system of TOF-PET consists of the outer ring detector of Fig.8. The radius of the ring is $d + h = d_0$ = 20 cm and the length in the z-axis is also $2z_0$ = 20 cm. It is made of BaF_2 scintillation material.

The efficiency of a γ-camera based SPECT for a point source in air is given by the product of the solid-angle fraction f_a of lead collimator and the efficiency η_a of $NaI(Tl)$, $P_{spect} = f_a \eta_a$. If the energies of the two coincidence photons in PP-SPECT are in the range of 100-200 Kev, $\eta_a \approx 1$, i.e., the photons that pass through the collimator are all detected. The expression for the factor f_a is given by [7,12]:

$$f_a = \left[\frac{\kappa t_a^2}{l_a (t_a + \tau_a)}\right]^2 \tag{9}$$

where κ = 0.282, t_a is the hole diameter, l_a is the thickness, and τ_a is the septal thickness of the collimator. Using the values given in table 3 and assuming τ_a = 0.75 mm, the efficiency of PP-SPECT is (for the truncated spherical detector of five γ-cameras) $P_{pp\text{-}spect} = (5 P_{spect})^2 = 0.2034 \times 10^{-6}$. The value of $P_{pp\text{-}spect}$ will be increased if the truncated spherical detector of Fig.5 is used, in which the thin detector is replaced by lead collimator and the thick detector is made of $NaI(Tl)$.

The efficiency of TOF-PET for the point source in air at the center of the multiple-slice detector [31] (i.e., outer ring of Fig.8) with radius d_0 and length $2z_0$ is:

$$P_{tof\text{-}pet} = f_b P_A P_A \eta_b^2 \tag{10}$$

where the solid-angle fraction $f_b = 67\% z_0/\sqrt{d_0^2 + z_0^2}$ = 29.96% for d_0 = 20 and z_0 = 10 cm [10,31]; the probability P_A of photoelectric absorption of incident primary photons in the thick detector (for BGO) is assumed to be 75% [15]; and the factor η_b is the ratio of efficiency between BaF_2 and BGO, η_b = 60%/77% [15]. The efficiency of TOF-PET is $P_{tof\text{-}pet}$ = 10.23%.

The efficiency of TPCIT is determined by the likelihoods of the multi-fold coincidence interactions of Figs.4 and 9.

The likelihood of the coincidence event of a single-photon undergoing electronic collimation of the thin-thick detector stack of Fig.4 is (for normal incident photons on a thin-detector element):

$$P_0(E) = P_{A0} P_{cp} \tag{11}$$

where P_{cp} is the probability of a single Compton scattering of incident photons in the thin detector and P_{A0} the probability of absorption in the thick detector of a photon that was Compton scattered in the thin detector.

The likelihoods of each of the coincidence events of pair-photons from positron annihilation, as shown by Fig.9, are:

$$P_1 = P_a P_a, \quad P_2 = P_A P_a, \quad P_3 = P_A P_A \tag{12}$$

$$P_4 = P_{A0} P_{cp} P_a$$

$$P_5 = P_{A0} P_{cp} P_A, \quad P_6 = P_{A0} P_{cp} P_{cp} P_{A0}$$

where P_a is the probability of photoelectric absorption of incident primary photons in the thin detector and P_A has been defined before. The values of P_{cp} and P_a associated with the thin detector are calculated based on the three physical interactions of photoelectric absorption, inelastic Compton and Rayleigh scattering within the thin-detector element. The mathematical expressions of the probabilities for these interactions are [10,12]:

$$P_{cp}(E,l) = \int_0^l dx \left[u_{cp} e^{-ux}\right] \int_{\theta_{min}}^{\theta_{max}} \sigma(\theta, E)\, d\theta\, e^{-u(E) L(x,\theta)}$$

$$P_a(E,l) = \frac{u_a}{u}\left(1 - e^{-ul}\right) \tag{13}$$

where u_{cp}, u_a and u are the linear attenuation coefficients of inelastic Compton scattering, photoelectric effect and total of the three interactions, respectively, for incident photons in $HpGe$, $u(E)$ is the linear attenuation coefficient in the thin detector of the scattered photons with energy E [34]. θ_{min} and θ_{max} are the scatter-angle limits determined by the energy resolution of the thin-detector element and the geometry of the detector stacks [12]. The values of P_A and P_{A0} associated with the thick detector can be obtained by use of a Monte Carlo method [15,34]. The values of P_{cp}, P_a, P_{A0} and P_i of Eq.(12) are given in Appendix.

The efficiency of u-TPCIT for a point source in air at the center of the detector system of Fig.5 is:

$$P_{u\text{-}tpcit} = [P_0(224) f_u]\,[P_0(344) f_u]\,[P_0(455) f_u] \tag{14}$$

where f_u is the solid-angle fraction for the single-photon detection, $P_0(E)$ was defined by Eq.(11), and E = 224, 344, or 455 Kev as given in Fig.6. f_u = 87.27% for the truncated spherical detector of Fig.5 with d = 15 and b = 10 cm, and then $P_{u\text{-}tpcit} = 4.1193 \times 10^{-4}$. The ratio of efficiency for u-TPCIT and PP-SPECT is ρ_a = 2025. It is noted that ρ_a would be smaller if the random coincidences of u-TPCIT are considered, or the PP-SPECT uses the truncated spherical detector system in which the inner thin detector is replaced by lead collimators.

The efficiency of c-TPCIT for the point source in air at the center of the truncated spherical detector of Fig.5 is:

$$P_{c\text{-}tpcit} = [P_0(168) f_u] (\sum_{i=1}^{6} P_i f_c) \quad (15)$$

where f_c = 74.54% is the solid-angle fraction for pair-photons [10], and $P_{c\text{-}tpcit}$ = 2.6006%. The ratio of efficiency for c-TPCIT and TOF-PET is ρ_b = 25.42%. If TOF-PET uses the truncated spherical detector, ρ_b would be smaller.

If the point source is at the center of a spherical water phantom with radius of 10 *cm* centered within the detector systems, rather than in air, the ratio ρ_a is reduced to 1397 and ρ_b is reduced to 6.05%.

SYSTEM SENSITIVITY FOR WATER PHANTOM

The sensitivity of multiple-photon coincidence detection for a water phantom is determined by the general formula [9-10,12] for a thin-detector element or a collimator hole:

$$S = \iiint \eta [c\, dv] \{ \frac{da}{4\pi R^2} \cos(\psi) e^{-uL} \} P_p\, dv, \quad (16)$$

where η is the probability of a coincidence detection for a single- or pair-photon event, c the radioisotope concentration of the water phantom, da the area of a detector element or a collimator hole, and R the distance from emission site to the thin-detector element; ψ is the angle between R and da, u the linear attenuation of water, and L the intersection length of a projection ray and the water phantom for a pair-photon coincidence detection or the distance of a photon traveling through within the water phantom for a single-photon detection; P_p represents the likelihood of the other photon (for PP-SPECT and TOF-PET), or the other two photons (for u-TPCIT), or the single-photon (for c-TPCIT) emitted at the position dv and detected simultaneously by the detector system.

If the water phantom is a sphere with radius r_0 = 10 *cm* and is centered within the truncated spherical detector system of Fig.5, Eq.(16) is expressed, in spherical coordinates (r, θ, ϕ), as:

$$S = (\frac{\eta c\, da}{4\pi}) \int_0^{2\pi} d\phi \int_0^{\pi} d\theta \int_0^{r_0} dr\ r^2 \sin(\theta) (\frac{\cos(\psi)}{R^2}) \times e^{-uL} P_p(r, \theta, \phi) \quad (17)$$

where the thin-detector element da is located at $y = z = 0$ and $x = d$, d is the distance from the thin-detector element to the center of the spherical water phantom (i.e., d is the inner radius of the detector system as defined before); $R^2 = d^2 + r^2 - 2\,d\,r \sin(\theta) \cos(\phi)$, and $\cos(\psi) = [d - r \sin(\theta) \cos(\phi)] / R$. For u-TPCIT:

$$L = R - d\cos(\psi) + \sqrt{(d\cos(\psi))^2 - (d^2 - r_0^2)} \quad (18)$$

$$P_p(r, \theta, \phi) = \prod_{i=1}^{2} P_{ip} = \prod_{i=1}^{2} \eta_i \int_{\Omega} \frac{da_i}{4\pi R_i^2} \cos(\psi_i) e^{-u_i L_i} \quad (19)$$

where da_i integrates over the whole surface Ω of the truncated spherical thin detector; R_i, L_i, u_i and ψ_i have the same meanings as R, L, u and ψ respectively. For c-TPCIT:

$$L = 2\sqrt{(d\cos(\psi))^2 - (d^2 - r_0^2)} \ \&\ P_p(r, \theta, \phi) = P_{ip}. \quad (20)$$

To simplify the calculation, assuming that the value of P_{ip} is, for the spherical water phantom, approximated by:

$$P_{ip} = \eta_i f_u < exp(-u_i L_i) >, \quad (21)$$

then Eq.(17) becomes:

$$S = (\frac{\eta c\, da}{4\pi} P_p) [\int_0^{2\pi} d\phi \int_0^{\pi} d\theta \int_0^{r_0} dr\ r^2 \sin(\theta) \times (\frac{\cos(\psi)}{R^2}) e^{-uL}]. \quad (22)$$

The integral values in the square parenthesis of Eq.(22), the probabilities η_i and P_{ip} in Eq.(21) are given in the Appendix.

The sensitivity of a detector element of u-TPCIT, for the spherical water phantom, is:

$$S_{u\text{-}tpcit}(da) = (\frac{c\, da}{4\pi}) \{ \eta_1(224) S_1[224] \} P_{2p}(344) P_{3p}(455) = (c\, da) \times 3.7787 \times 10^{-5} \quad (23)$$

where $\eta_i(.)$, $S_i[.]$ and $P_{ip}(.)$ for different energies are given in the Appendix.

The sensitivity of a detector element for c-TPCIT is:

$$S_{c\text{-}tpcit}(da) = (\frac{c\, da}{4\pi}) \{ \eta_5(511) S_4[511] \} P_{4p}(168) = (c\, da) \times 3.1483 \times 10^{-3}. \quad (24)$$

In the PP-SPECT mode, since the size of collimator holes is very small, Eq.(16) can be approximately expressed as (for a collimator hole) [12]:

$$S_{pp\text{-}spect}(da) = \eta \frac{c\, da}{2u} P_p \int_0^{\theta_0} \cos(\theta)\, d\cos(\theta) \times [exp(-2\,u\, r_0/\cos(\theta)) - 1] \quad (25)$$

where $\tan(\theta_0) = t_a / (2\, l_a)$, u = 0.1537 cm^{-1}, and $\eta \approx 1$ (i.e., the γ-camera has 100% efficiency to absorbe the photons passed through the collimator). For PP-SPECT consisting of 5 γ-cameras, $P_p = 5\, P_{spect}\, e^{-1.537}$. The integral value of Eq.(25) is given by [10]:

$$S_{pp\text{-}spect}(da) = (c\, da) \times 3.1113 \times 10^{-7}. \quad (26)$$

For the multiple-slice ring detector of TOF-PET with radius of d_0 and length of $2z_0$ [31], a cylindrical water phantom with radius of r_0 and length of $2z_0$ is considered (i.e., the geometry of this water phantom and the multiple-slice detector is equivalent to that of the spherical water phantom and the truncated spherical detector), and Eq.(16) becomes:

$$S_{tof\text{-}pet}(da) = [\frac{\eta c\, da}{\pi}] \int_0^{\pi} d\phi \int_0^{r_0} dr \int_0^{z_0} dz \times [\frac{r(d_0 - r\cos(\phi))}{R^{3/2}}] e^{-uL} \quad (27)$$

where $R^2 = d_0^2 + z^2 + r^2 - 2\,d_0\,r\cos(\phi)$, $L = 2\,R\,L_0$, and

$$L_0 = \frac{\sqrt{d_0^2(d_0 - r\cos(\phi))^2 - (d_0^2 - r_0^2)(R^2 - z^2)}}{R^2 - z^2}. \quad (28)$$

The integral value is given by [14]:

$$S_{tof\text{-}pet}(da) = (c\ da) \times 1.4295 \times 10^{-2}. \quad (29)$$

The ratio of sensitivity for u-TPCIT and PP-SPECT for the water phantom detection is:

$$\rho_c = [f_u\, S_{u\text{-}tpcit}(da)] / [f_u\, S_{pp\text{-}spect}(da)] = 121,$$

i.e., u-TPCIT has higher sensitivity than PP-SPECT. As discussed previously, u-TPCIT is expected to generate better images than PP-SPECT.

The ratio of sensitivity for c-TPCIT with the truncated spherical detector and TOF-PET with the multiple-slice ring detector [31] for the water phantoms is:

$$\rho_d = [f_u\, S_{c\text{-}tpcit}(da)] / [f_b\, S_{tof\text{-}pet}(da)] = 64.14\%.$$

If c-TPCIT uses the double-ring detector of Fig.8 and TOF-PET uses the outer-ring detector, the ratio of sensitivity is $\rho_{dd} = S_{c\text{-}tpcit}(da) / S_{tof\text{-}pet}(da) = 22.02\%$. c-TPCIT improves significantly the localization range, as compared with TOF-PET, at the cost of lower sensitivity. For a first-order approximation, the gain achieved in image quality by using c-TPCIT (compared with TOF-PET) may be expressed, with the ratio of sensitivity and localization range, as [32]:

$$\varsigma = \frac{S_{c\text{-}tpcit} / I_{c\text{-}tpcit}}{S_{tof\text{-}pet} / I_{tof\text{-}pet}} = \left(\frac{S_{c\text{-}tpcit}}{S_{tof\text{-}pet}}\right)\left(\frac{I_{tof\text{-}pet}}{I_{c\text{-}tpcit}}\right). \quad (30)$$

The gain is $\varsigma = 4.49$ for c-TPCIT with the truncated spherical detector of Fig.5 and TOF-PET with the multiple-slice ring detector [31]. The gain ς reduces to 1.54 if both c-TPCIT and TOF-PET use the same detector geometry of Fig.8. It is anticipated that c-TPCIT would produce improved images, as compared to TOF-PET.

DISCUSSION

We have discussed multiple-photon coincidence imaging techniques. In the TPCIT imaging modes, electronic collimation of the scattering-absorption detecting process [10-12] provides the possibility of utilizing the single-photon information to improve the localization range of a PET system while maintaining a reasonable sensitivity. It also provides the possibility to directly reconstruct images from projections mapped one-to-one onto small volumes by angularly unconstrained triple-photon coincidence events with reasonable sensitivity.

This paper provided analytical comparisons of u-TPCIT with PP-SPECT and c-TPCIT with TOF-PET. Their advantages and limitations were discussed. Although the calculations did not include the effects of random coincidence and multiple Compton scattering in the thin and thick detectors, the numerical results qualitatively reflected the essential properties of u-TPCIT and c-TPCIT. The cost of TPCIT is also an important factor that should be considered.

The relatively lower sensitivity with the TPCIT modes can be improved if more than one single-photons (for c-TPCIT) or more than three single-photons (for u-TPCIT) are emitted by the radioisotopes simultaneously [30].

It should be emphasized that the essential motivation of the TPCIT is to increase the localization information of projections with acceptable sensitivity. In the ideal situation, the image would be reconstructed from points rather than from lines. The net gain between increased localization range and compromised sensitivity requires further investigation. The signal-to-noise characteristics of these imaging techniques can be modeled using Monte Carlo simulations.

APPENDIX

The values of P_{cp}, P_a, P_{A0} and P_i defined in Eqs.(11)-(13) are given below. For $l = 6\ mm$ as used in the section on spatial resolution, $P_a = 0.90\%$, and

$$P_{cp}(168) = 6.50\%,\ P_{cp}(224) = 8.21\%,$$
$$P_{cp}(344) = 9.86\%,\ P_{cp}(455) = 10.09\%,$$
$$P_{cp}(511) = 10.03\%$$

where the values in parenthesis are referred to the energies of the photons, respectively. $P_{A0} = 80\%$ is chosen for photons with energy $> 500\ Kev$. P_{A0} increases to 100% as the photon energy decreases to 100 *Kev*. The values of P_{A0} for different photon energies are:

$$P_{A0}(168) = 96.9\%,\ P_{A0}(244) = 94.2\%,$$
$$P_{A0}(344) = 90.1\%,\ P_{A0}(455) = 89.4\%.$$

The likelihoods of the different pair-photon events given by Eq.(12) are:

$$P_1 = 0.000081,\ P_2 = 0.006750,\ P_3 = 0.562500.$$
$$P_4 = 0.000722,\ P_5 = 0.060180,\ P_6 = 0.006439$$

The integral values in the square parenthesis of Eq.(22) are:

$$S_1[224] = 8.3061,\ S_2[344] = 9.1543,$$
$$S_3[455] = 9.7831,\ S_4[511] = 4.7615.$$

The probabilities of η_i in Eq.(21) are:

$$\eta_1(224) = P_{cp}(224)\,P_{A0} = 7.73\%$$
$$\eta_2(344) = P_{cp}(344)\,P_{A0} = 8.88\%$$
$$\eta_3(455) = P_{cp}(455)\,P_{A0} = 9.02\%$$
$$\eta_4(168) = P_{cp}(168)\,P_{A0} = 6.28\%$$
$$\eta_5(511) = \sum_{i=1}^{6} P_i = 63.67\%.$$

Assuming that the average $< exp(-u_i L_i) > = exp(-u_i r_0)$, the values for P_{ip} of Eq.(21) are:

$$P_{1p}(224) = 1.7753\%, \quad P_{2p}(344) = 2.5539\%$$

$$P_{3p}(455) = 2.8958\%, \quad P_{4p}(168) = 1.3050\%.$$

REFERENCES

[1] M. Phelps, E. Hoffman, et al: "Application of Annihilation Coincidence Detection to Transaxial Reconstruction Tomography." J. Nucl. Medicine, vol.16, no.3, pp.210-224, 1975

[2] M. Phelps: "Emission Computed Tomography." Seminars in Nucl. Medicine, vol.7, no.3, pp.337-365, 1977

[3] T. Budinger: "Physical Attributes of SPECT." J. Nucl. Medicine, vol.21, no.6, pp.576-592, 1980

[4] R. Jaszczak, R. Coleman, et al: "SPECT: Single photon emission computed tomography." IEEE Trans. Nucl. Sci., vol.27, no.3, pp.1137-1153, 1980

[5] W. Wong, N. Mullani, et al: "Image Improvement and Design Optimization of the Time-of-Flight PET." J. Nucl. Medicine, vol.24, no.1, pp.52-60, 1983

[6] H. Boetticher, H. Helmers, et al: "Gamma-Gamma-Coincidence Scintigraphy: Tomography without computerized image reconstruction." in *Medical Radionuclide Imaging*, vol.1, (IAEA, Vienna), pp.147-148, 1980

[7] H. Anger: "Radioisotope Cameras." in *Instrumentation in Nuclear Medicine*, Academic, NY, USA, 1967

[8] H. Hart and S. Rudin: "Three Dimensional Imaging of Multi-millimeter Sized Cold Lesions by Focusing Collimator Coincidence Scanning (FCCS)." IEEE Trans. Biomed. Engin., vol.24, no.2, pp.169-177, 1977

[9] Z. Liang, H. Hart and A. Schoenfeld: "Triple Gamma Coincidence Tomographic Imaging without Image Processing." Proc. IEEE, Engineering in Medicine and Biology Society, Boston, MA, vol.9, pp.825-826, 1987.

[10] Z. Liang: "Preliminary Study of Triple Photon Coincidence Imaging Technique." Proc. SPIE, Applications of Digital Image Processing XI, San Diego, CA, vol.974, pp.283-291, 1988

[11] A. Zych, R. Wilson, et al: "Double Scatter Telescope for Medium Energy Gamma Ray Astronomy from a Satellite." IEEE Trans. Nucl. Sci., vol.26, no.1, pp.506-512, 1979

[12] M. Singh: "An Electronically Collimated Gamma Camera for SPECT. Part 1: theoretical considerations and design criteria." Medical Physics, vol.10, no.4, pp.421-427, 1983

[13] Z. Liang: "Utilization of Single Photon in PET." Proc. ACEMB on Engineering in Medicine and Biology, Niagara Falls, NY, vol.40, pp.213, 1987

[14] Z. Liang: "Analytical Study of a Three Dimensional Imaging System using Both Single and Coincident Pair Photons." Proc. IEEE Southeastcon'89 on Energy and Information Technologies, Columbia, SC, no.3, pp.1085-1092, 1989

[15] S. Derenzo: "Comparison of Detector Materials for Time-of-Flight Positron Tomography." Proc. IEEE Computer Society, Workshop on Time-of-Flight Tomography, St. Louis, MO, no.448, pp.63-68, 1982

[16] J. Llacer and Z. Cho: "Preliminary Study of a Germanium 3D Camera for Positron Emitting Radioisotopes." IEEE Trans. Nucl. Sci., vol.20, no.1, pp.282-293, 1973

[17] J. Bieszk, C. Lim and E. Hawman: "A Method of Improving Photon Detection Efficiency of High Purity Germanium Cameras by Including Double Interaction Photopeak Events." IEEE Trans. Nucl. Sci., vol.30, no.1, pp.586-590, 1983

[18] J. Detko: "A Prototype, Ultra Pure Germanium, Orthogonal Strip Gamma Camera." Proc. IAEA on Radioisotope Scintigraphy, Monte Carlo, SM-164/135, 1972

[19] L. Kaufman, S. Williams, et al: "An Evaluation of Semiconductor Detectors for Positron Tomography." IEEE Trans. Nucl. Sci., vol.26, no.1, pp.648-653, 1979

[20] P. Schlosser, D. Miller, et al: "A Practical Gamma Ray Camera System using High Purity Germanium." IEEE Trans. Nucl. Sci., vol.21, no.1, pp.658-664, 1974

[21] P. Lyons, S. Caldwell et al: "Sub-Nanosecond Plastic Scintillators." IEEE trans. Nucl. Sci., vol.24, no.1, pp.177-181, 1977

[22] J. McLntyre: "Plastic Scintillators for Time-of-Flight Tomography." Proc. IEEE Computer Society, Workshop on Time-of-Flight Tomography, St. Louis, MO, no.448, pp.51-58, 1982

[23] J. Alberi: "Position Readout by Charge Division in Large 2D Detectors." IEEE Trans. Nucl. Sci., vol.24, no.1, pp.188-194, 1977

[24] G. Muehllehner and J. Karp: "A Positron Camera using Position Sensitive Detectors: PENN-PET." J. Nucl. Medicine, vol.27, no.1, pp.90-98, 1986

[25] M. Singh, R. Leahy, et al: "Noise Propagation in Electronically Collimated Single Photon Imaging." IEEE Trans. Nucl. Sci., vol.35, no.1, pp.772-777, 1988

[26] C. Lederer and V. Shirley: *Table of Isotopes.* John Wiley & Sons, Inc., NY, USA, 1978

[27] T. Lewellen, A. Bice, et al: "Performance Measurements of the SP3000/UW Time-of-Flight PET." IEEE Trans. Nucl. Sci., vol.35, no.1, pp.665-669, 1988

[28] D. Ficke, D. Beecher, et al: "TOF Acquisition: System design and experimental results." Proc. IEEE Computer Society, Workshop on Time-of-Flight Tomography, St. Louis, MO, no.448, pp.139-141, 1982

[29] H. Spieler: "Fast Timing Methods for Semiconductor Detectors." IEEE Trans. Nucl. Sci., vol.29, no.3, pp.1142-1158, 1982

[30] H. Hart: "Multiple Gamma and Positron-Gamma Coincidence Imaging." Proc. IEEE, Engineering in Medicine and Biology Society, Boston, MA, vol.9, pp.1340-1341, 1987

[31] E. Tanaka, N. Nohara, et al: "Analytical Study of the Performance of a Multilayer PET Scanner." J. Comput. Assist. Tomography, vol.6, no.2, pp.350-364, 1982

[32] Private communication with Dr. S. Derenzo and Dr. M. Yamamoto

[33] Triad SPECT Operation Manual, TRIONIX Research Laboratory, Inc., Ohio, USA, 1988

[34] E. Storm and H. Israel: "Photon Cross Section from 1 *Kev* to 100 *Mev* for Elements z=1 to z=100." Nucl. Data Tables, vol.7, no.A, pp.565-681, 1970